12

Reprinted from JOURNAL OF THE ATMOSPHERIC SCIENCES, Vol. 45, No. 23, 1 December 1988
American Meteorological Society

Normal Mode Energetics of the General Circulation during the FGGE Year*

H. L. TANAKA** AND ERNEST C. KUNG

Department of Atmospheric Science, University of Missouri-Columbia, Columbia, Missouri

(Manuscript received 24 August 1987, in final form 24 June 1988)

ABSTRACT

Three-dimensional normal mode functions are applied to the analysis of the energetics of the general circulation during the FGGE year. The GFDL FGGE data are used for the computation of both the normal mode energetics and the standard spectral energetics.

The normal mode energetics of the global circulation are presented in a barotropic and baroclinic decomposition for the zonal mean and eddy energies for the stationary and transient components of the flow. The energy generated in the zonal mean baroclinic component is first transformed to the eddy baroclinic component through the process of atmospheric baroclinic instability. It is then further transformed to eddy and zonal mean barotropic components by the nonlinear up-scale cascade of kinetic energy. The zonal mean kinetic energy thus maintains its barotropic structure by the activities of baroclinic waves. The time series of energy variables during the FGGE Northern Hemisphere winter clearly indicates a sequence of energy transformations from the zonal baroclinic component via the synoptic-scale baroclinic component, to the planetary-scale barotropic component.

Comparison of the normal mode energetics with the standard spectral energetics in the zonal wavenumber domain indicates a general consistency of both schemes in the spectral energy transformations.

1. Introduction

Energetics of the atmospheric general circulation has been investigated with orthogonal projections of the circulation field onto various basis functions, which includes spectral energetics schemes using a zonal harmonic expansion (Saltzman 1957, 1970), a spherical harmonic expansion in the zonal and meridional directions (Eliasen and Machenhauer 1965), and empirical orthogonal functions in the vertical direction (Holmström 1963). Three-dimensional normal mode functions (3-D NMFs) introduced by Kasahara and Puri (1981) are orthonormal functions which can be used as an expansion basis for the global energetics analysis (Tanaka 1985). The three-dimensional normal mode energetics combines the three one-dimensional spectral energetics in domains of zonal wavenumbers, a meridional index, and a vertical index. The scheme can diagnose not only the three-dimensional spectral distribution of energy and energy transformations but also the energetics characteristics of Rossby waves and gravity waves and the energy conversion between the barotropic and baroclinic modes.

A comparative normal mode energetics diagnosis was performed for a winter month by Tanaka et al. (1986) using the First GARP (Global Atmospheric Research Program) Global Experiment (FGGE) analysis datasets prepared by the Geophysical Fluid Dynamics Laboratory (GFDL) and the Goddard Laboratory for Atmosphere (GLA). The analysis, however, only involved a winter month. The extent of analysis was also limited because of its preliminary nature. It is desirable then to present the comprehensive normal mode energy budget for the entire FGGE year with an expanded analysis scheme. The present analysis includes the evaluation of energy flow in the normal mode projection, further decomposition of the energy budget into the stationary and transient components, and time series analysis with a focus on the conversion between baroclinic and barotropic components of different scales.

It should be noted that the assumptions and the specific computational procedures involved in the normal mode energetics scheme may cause an inherent bias in the energetics statistics. For example, the standard spectral energetics in the zonal wavenumber domain utilizes the temperature variance for the evaluation of available potential energy. In the normal mode energetics the perturbation geopotential is expanded in the vertical structure functions, and the available potential energy is evaluated by the square sum of the expansion coefficients. Another example is that the numerical solutions of the vertical structure equation have a problem of aliasing in the higher order baroclinic modes, resulting in a misleading profile in the stratosphere and

* Contribution from the Missouri Agricultural Experiment Station, Journal Series No. 10396.

** Present affiliation: Geophysical Institute, University of Alaska-Fairbanks, Fairbanks, Alaska.

Corresponding author address: Dr. Ernest C. Kung, Department of Atmospheric Science, University of Missouri-Columbia, Columbia, MO 65211.

above (Sasaki and Chang 1985; Fulton and Schubert 1985; Staniforth et al. 1985). Also, the data projection onto these functions imposes the boundary condition of the 3-D NMFs not only for transient waves but also for steady atmospheric fields which may take arbitrary boundary structures. Energetics results of the steady field thus might be affected by the data projection onto the vertical structure functions. In fact, the contribution to available potential energy has a large concentration near the surface, implying a possible distortion in the rapid change of geopotential field (e.g., Tenenbaum 1976). It is desirable to examine energetics characteristics of steady and transient atmospheric fields, and to compare the results with the standard spectral energetics. Physically it is also preferable to examine the barotropic and baroclinic components of energy variables of transient fields of motion.

The three-dimensional normal mode energetics can complement the standard spectral energetics analysis in the zonal wavenumber domain to produce a comprehensive understanding of the general circulation. In this study, the normal mode energetics of the general circulation are analyzed for the FGGE year using the Level IIIb GFDL dataset. Results of the analysis are summarized, based on the barotropic and baroclinic decompositions of zonal and eddy energies for the stationary and transient flows of the circulation. Further, a time series analysis is presented for the energy components and energy transformations to explore nonlinear transformations among the different scales of baroclinic and barotropic components. Some pertinent comparisons of the normal mode energetics and the standard spectral energetics are also made with the same GFDL database.

2. Data and analysis scheme

This study utilizes the GFDL IIIb dataset of the FGGE observations (twice daily at 0000 and 1200 UTC), for a one-year period from 1 December 1978 through 30 November 1979 (see Miyakoda et al. 1982; Ploshay et al. 1983). The original GFDL analysis data at 1000, 850, 700, 500, 400, 300, 250, 200, 150, 100, 50 and 30 mb on a 1.875° by 1.875° grid were interpolated to a 4° by 5° grid from 90°S to 90°N and from 0°E to 355°E, as described by Kung and Tanaka (1983).

The analysis scheme of the normal mode energetics has been detailed in Tanaka (1985) and Tanaka et al. (1986). The description of the scheme is summarized in the Appendix with some modifications to the original scheme. First, the vertical structure functions and the Hough harmonics are computed, using a reference state of the global mean temperature averaged for the FGGE year (see Table 1 of Tanaka 1985). Sets of vertical and Fourier-Hough transforms are then constructed based on the orthonormality of the eigenfunctions (refer to Kasahara and Puri 1981). For the computation of the Hough functions, 60 Gaussian latitudes were chosen. The energetics terms computed at every 4° of latitude are interpolated to the Gaussian latitudes after the vertical transform has been performed.

Applied to a sequence of vertical and Fourier-Hough transforms with proper scaling factors, the spectral representation of the primitive equations becomes a system of ordinary, dimensionless differential equations:

$$\frac{d}{d\tilde{t}} w_{nlm} + i\sigma_{nlm} w_{nlm} = b_{nlm} + c_{nlm} + d_{nlm}, \quad (1)$$

where the complex variables w_{nlm}, b_{nlm}, c_{nlm}, and d_{nlm} represent the vertical and Fourier-Hough transforms of the variables: w_{nlm} for the horizontal wind and perturbation geopotential, b_{nlm} for the nonlinear terms due to the wind field, c_{nlm} for the nonlinear terms due to the mass field, and d_{nlm} for the diabatic processes including friction (see Tanaka 1985). The symbol i is the imaginary unit, and σ_{nlm} is the dimensionless eigenfrequency obtained as a solution of Laplace's tidal equation, with a basic state at rest. The subscripts n, l, and m are for the zonal wavenumber, meridional index, and vertical index, respectively. (See Table 1 for symbols, definitions, and variables in this text.) The vertical modes $m = 0$ and $m = 1$–11 are regarded as the barotropic (external) and baroclinic (internal) modes, respectively (see Tanaka et al. 1986, for their structures). The zonal wavenumber has been truncated at $n = 15$. We have used a total of 50 meridional indices, including 26 Rossby modes and 12 eastward and 12 westward gravity modes.

The corresponding energy balance equation in the dimensional form is given by

$$\frac{d}{dt} E_{nlm} = B_{nlm} + C_{nlm} + D_{nlm}, \quad (2)$$

where

$$E_{nlm} = \frac{1}{2} p_s h_m |w_{nlm}|^2, \quad (3)$$

$$B_{nlm} = \Omega p_s h_m (w^*_{nlm} b_{nlm} + w_{nlm} b^*_{nlm}), \quad (4)$$

$$C_{nlm} = \Omega p_s h_m (w^*_{nlm} c_{nlm} + w_{nlm} c^*_{nlm}), \quad (5)$$

$$D_{nlm} = \Omega p_s h_m (w^*_{nlm} d_{nlm} + w_{nlm} d^*_{nlm}). \quad (6)$$

The dimensional factors h_m, Ω, and p_s are respectively the equivalent height, angular speed of earth's rotation, and surface pressure which is treated as a constant (1013 mb). The asterisk denotes the complex conjugate here. According to Eq. (2), the time change of the total energy E_{nlm} defined by Eq. (3) is caused by the nonlinear mode-mode interaction among kinetic energy B_{nlm}, available potential energy C_{nlm}, and a net energy source and sink due to the diabatic process D_{nlm}, which includes dissipation. The kinetic energy K_{nlm} and the available potential energy P_{nlm} of each mode can be

TABLE 1. Symbols, definitions, and variables.

n	Zonal wavenumber
l	Meridional index
m	Vertical index
K	Kinetic energy
P	Available potential energy
E	Total energy: $E = K + P$
L	Wave-wave interaction of K
M	Wave-mean interaction of K
S	Wave-wave interaction of P
R	Mean-mean interaction of P
B	Nonlinear interaction of K: $B(n) = L(n) - M(n)$
C	Nonlinear interaction of P: $C(n) = S(n) + R(n)$
D	Net energy source and sink due to diabatic process including frictional dissipation
T_0	Reference state temperature
T	Temperature deviation from T_0
ϕ	Geopotential deviation from its reference state
p_s	Surface pressure of the reference state
$\vec{V}$	Horizontal wind velocity
ω	Vertical p-velocity ($=dp/dt$)
g	Earth's gravity
a	Earth's radius
Ω	Angular speed of earth's rotation
h_m	Equivalent height
t	Time
$\tilde{t}$	Dimensionless time scaled by 2Ω
∇	Horizontal del-operator
dz/dt	Vertical velocity
δ_{ij}	Kronecker delta
i	Imaginary unit
$\int (\ )dS$	Integral over the whole isobaric surface
$(\ )^T$	Transpose
$(\ )^*$	Complex conjugate
$(\ )_{nlm}$	A component of indices n, l, m
σ_{nlm}	Dimensionless eigenfrequency of Laplace's tidal equation
w_{nlm}	Expansion coefficient of dependent variable vector
b_{nlm}	Expansion coefficient of nonlinear term vector due to wind field
c_{nlm}	Expansion coefficient of nonlinear term vector due to mass field
d_{nlm}	Expansion coefficient of diabatic process including friction
$Q(t)$	Time dependent arbitrary meteorological variable
$(\ )_S$	Contribution from stationary component
$(\ )_A$	Contribution from annual cycle
$(\ )_T$	Contribution from transient component excluding an annual cycle

retrieved by E_{nlm} using the norm ratio of each Hough vector function. The diabatic process D_{nlm} is evaluated as the residual of Eq. (2).

By means of the inverse transforms of the vertical and Fourier-Hough transforms, it can be shown that

$$\sum_n \sum_l \sum_m B_{nlm} = \frac{1}{Sg}\int_S \int_0^{p_s} -\nabla \cdot K\mathbf{V} - \frac{\partial K\omega}{\partial p}\, dpdS = 0, \quad (7)$$

$$\sum_n \sum_l \sum_m C_{nlm} = \frac{1}{Sg}\int_S \int_0^{p_s} -\nabla \cdot P\mathbf{V} - \frac{\partial P\omega}{\partial p}\, dpdS = 0. \quad (8)$$

We have assumed in this study that the surface wind vanishes at the lower boundary of the atmosphere in order to obtain an energetically consistent set of equations (see Appendix). The right-hand sides of Eqs. (7) and (8) become zero under this assumption and a scaling of $T_0 \gg T$ even for the nonzero ω at the lower boundary.

Results of the energetics analysis presented in the subsequent sections are for the summations of Rossby and gravity modes unless otherwise stated. All of the energetics analyses were carried out on a global basis, except for the winter time series analysis, which was done with only the Northern Hemisphere data. The standard spectral energetics in the zonal wavenumber domain, which were compared with the normal mode energetics, were computed in accordance with the analysis scheme by Kung and Tanaka (1983) for the FGGE data.

3. Gross energy budget

The annual mean spectral distributions of kinetic energy and available potential energy as functions of the zonal wavenumber during the FGGE year are illustrated in Fig. 1. The results of the normal mode energetics (solid lines) are compared to those computed by the standard spectral energetics during the same period by Kung (1986) (dashed lines). The normal mode scheme yields smaller available potential energy

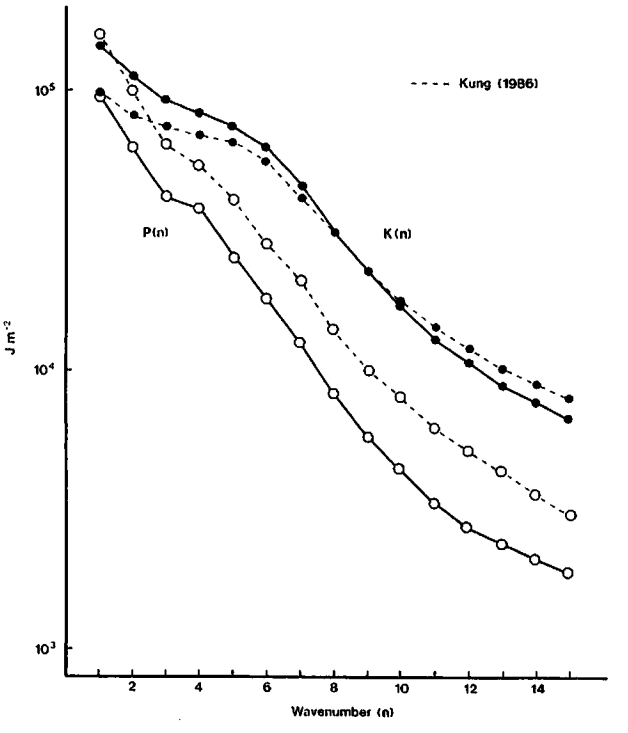

FIG. 1. Spectral distributions of kinetic energy and available potential energy in the wavenumber domain during the FGGE year by the normal mode scheme (solid line) and the standard spectral scheme after Kung (1986) (dashed line).

$P(n)$ for all wavenumbers than that of the standard spectral scheme. However, the normal mode energetics produces a greater kinetic energy for the long waves and a lesser kinetic energy for the short waves than the standard spectral scheme. The available potential energy was evaluated using a relation in the vertical structure equation, which has a second order derivative (see Kasahara and Puri 1981). The numerically solved vertical structure functions are known to have a problem of aliasing for the baroclinic modes, in which the available potential energy resides (e.g., Sasaki and Chang 1985; Staniforth et al. 1985). It has been suggested that the data projection onto the higher order vertical indices would lead to a misrepresentation in the energy level, even though the functions form an orthonormal basis in the vertical. Thus, the systematic bias of energy levels in the present scheme may have resulted partly from such an aliasing in the numerical vertical structure functions and partly from the effect of the lower boundary condition as discussed in the Introduction.

Despite the aforementioned discrepancy in the energy level, the present normal mode scheme has a specific advantage in decomposing the energy into Rossby and gravity modes. Figure 2 illustrates the annual mean spectral distribution of the total energy in the wavenumber domain for the Rossby mode and the eastward and westward gravity modes. The spectral distributions indicate a higher energy level of the eastward gravity mode for the long waves, especially for $n = 1$. The energy level of the gravity modes is very sensitive to the atmospheric ageostrophic components, and thus may be influenced by the assimilation process applied to the dataset. The results shown in Fig. 2 may provide baseline information for future diagnosis of analysis data or model simulations.

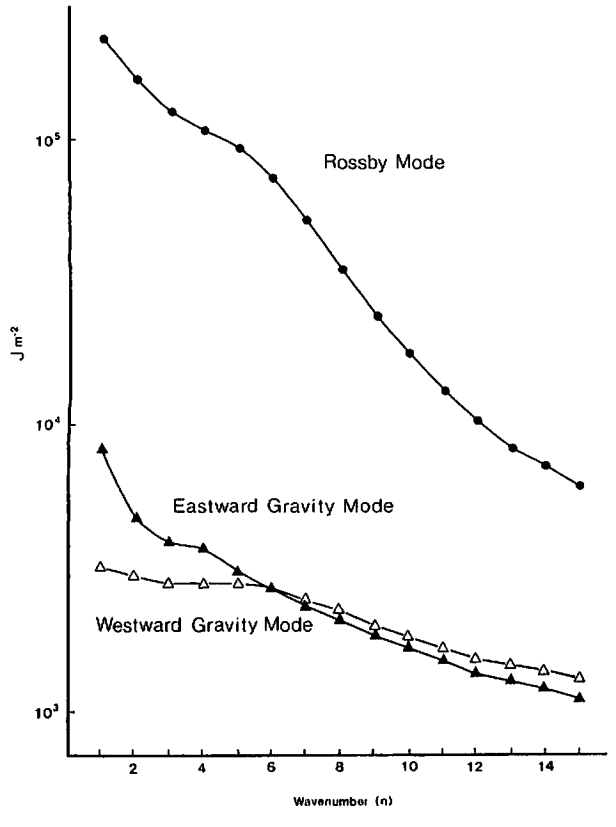

FIG. 2. Zonal energy spectra $E(n) = K(n) + P(n)$ for the Rossby mode, and eastward and westward gravity modes during the FGGE year.

In Fig. 3 the kinetic energy distributions for vertical indices $m = 0$–3 are plotted as functions of the dimensionless eigenfrequency (normalized by 2Ω), which is associated with each Hough harmonic. The eigenfrequency on the abscissa may be understood as the three-dimensional wave scale index. It should be noted that it differs from the wave frequency in space–time spectra as analyzed in Hayashi and Golder (1983). The left half of each diagram shows westward gravity modes and Rossby modes, and the right half shows eastward gravity modes. The distributions indicate clear kinetic energy peaks within the Rossby modes for each vertical index. The slope of the kinetic energy spectrum in the low-frequency Rossby modes approximately obeys the third power of the frequency. As was found in Tanaka (1985), the kinetic energy spectrum of the largest-scale Rossby mode merges with that of the largest-scale gravity mode, both for the baroclinic and barotropic modes. The highest kinetic energy levels in the right half of the diagram are marked by the Kelvin mode of $n = 1$ for the baroclinic indices. The energy level of the Kelvin mode for $m = 3$ is as large as the peak energy level in the Rossby modes. The higher energy levels of the eastward propagating gravity mode in planetary waves, as shown in Fig. 2, are clearly attributable to the internal Kelvin waves.

The results of the normal mode energetics during the FGGE year are summarized in Table 2 by the barotropic ($m = 0$) and baroclinic ($m = 1$–10) decomposition for zonal ($n = 0$) and eddy ($n = 1$–15) components. The annual mean budget (YEAR) is listed together with three month averages during December to February (DJF), March to May (MAM), June to August (JJA), and September to November (SON). The baroclinic energy is defined here by the summation of $m = 1$ to 10. The highest vertical index $m = 11$ is excluded to avoid the uncertainty of aliasing and noises. Although the summations of B, C, and D over all indices n, l, and m should ideally be zero, this condition is not met in the energy budget in Table 2. The discrepancy is caused by the assumptions that were discussed in the introduction, and by the truncations at $n = 15$ and $m = 10$. However, the energy budget is believed to correctly present the modal characteristics of the general circulation.

Zonal kinetic energy is characterized by its large barotropic component, whereas the zonal eddies contain a comparable amount of barotropic and baroclinic

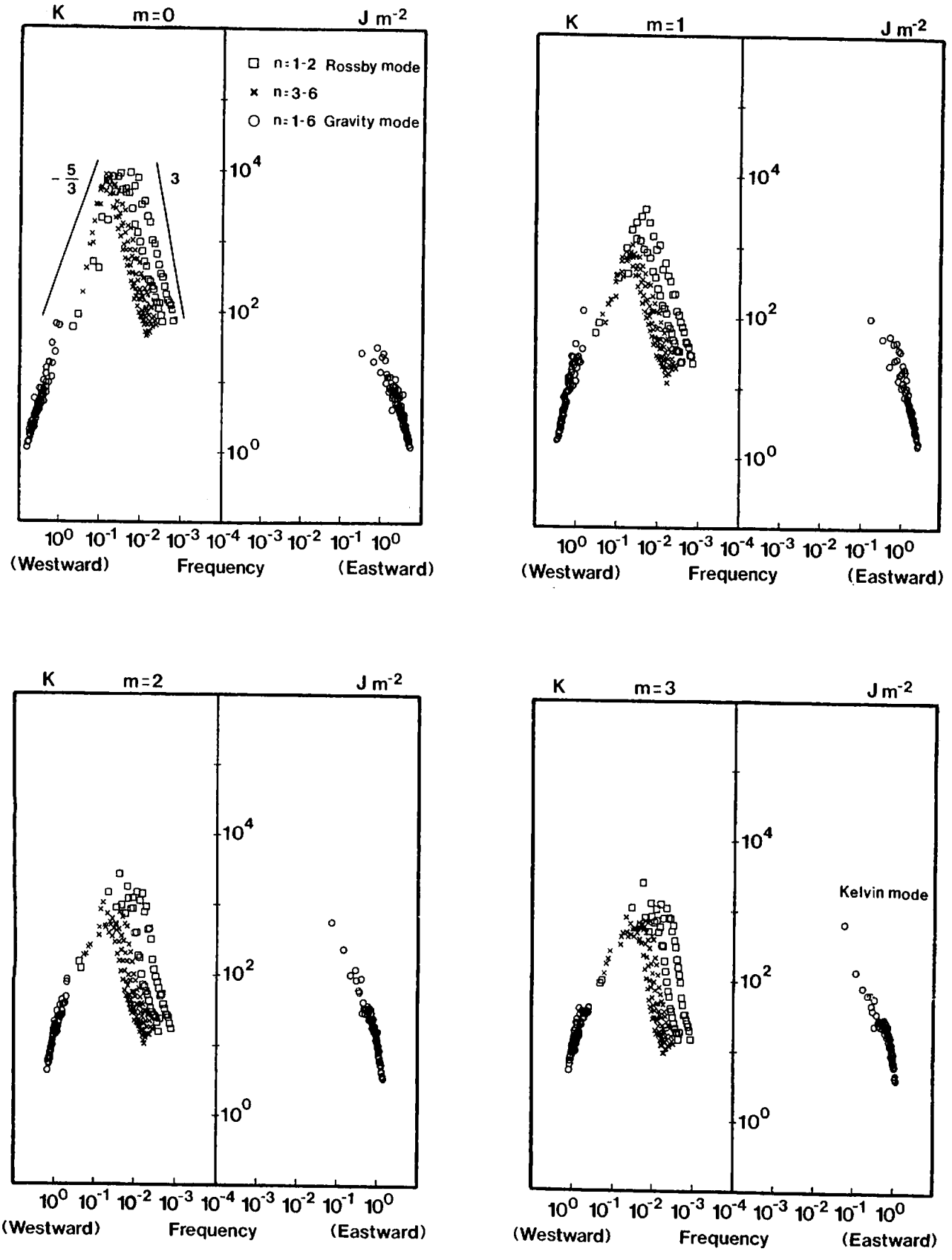

FIG. 3. Kinetic energy spectra in the dimensionless frequency domain (normalized by 2Ω) for vertical indices $m = 0$–3. The energy of the Rossby modes and gravity modes are plotted for wavenumber $n = 1$–6. Note that the frequency on the abscissa is the eigenfrequency of Laplace's tidal equation rather than the analyzed wave frequency in the space–time spectra.

TABLE 2. Mean normal mode energy budget during the FGGE year (YEAR), and three-month averages for December to February (DJF), March to May (MAM), June to August (JJA), and September to November (SON). Energies (K, P, and E) in unit of 10^5 J m^{-2} and energy transformations (B, C, and D) in W m^{-2} are listed for the zonal ($n = 0$) and eddy ($n = 1$–15) components by the barotropic ($m = 0$) and baroclinic ($m = 1$–10) decomposition.

n	m	K	P	E	B	C	D
YEAR							
0	0	6.9	2.4	9.3	0.39	−0.16	−0.23
0	1–10	3.8	40.6	44.5	−0.07	−1.47	1.54
1–15	0	3.3	0.2	3.5	0.32	0.10	−0.42
1–15	1–10	3.9	2.8	6.7	−0.75	1.46	−0.71
DJF							
0	0	6.5	1.9	8.4	0.47	−0.20	−0.27
0	1–10	4.1	44.2	48.3	−0.06	−1.85	1.97
1–15	0	3.6	0.2	3.8	0.33	0.10	−0.44
1–15	1–10	4.3	3.3	7.6	−0.82	1.63	−0.86
MAM							
0	0	6.3	2.0	8.3	0.38	−0.13	−0.24
0	1–10	3.6	40.1	43.7	−0.05	−1.41	1.32
1–15	0	3.4	0.2	3.6	0.30	0.10	−0.40
1–15	1–10	3.7	2.6	6.3	−0.73	1.44	−0.73
JJA							
0	0	7.6	3.5	11.1	0.33	−0.12	−0.18
0	1–10	3.7	38.3	42.0	−0.14	−1.07	1.29
1–15	0	2.9	0.2	3.0	0.30	0.08	−0.39
1–15	1–10	3.5	2.4	5.9	−0.59	1.11	−0.54
SON							
0	0	7.1	2.4	9.5	0.39	−0.18	−0.25
0	1–10	3.9	39.9	43.9	−0.02	−1.54	1.57
1–15	0	3.5	0.2	3.7	0.32	0.13	−0.44
1–15	1–10	4.0	2.8	6.8	−0.88	1.65	−0.73

kinetic energies. Available potential energy is concentrated in the zonal baroclinic components. There is a net energy generation in the zonal baroclinic components ($n = 0$, $m = 1$–10) by the dominant differential heating. The nonlinear interactions of available potential energy C indicate a large negative value in ($n = 0$, $m = 1$–10) and a positive value in ($n = 1$–15, $m = 1$–10), implying the available potential energy transformation from zonal baroclinic to eddy baroclinic components. The nonlinear interactions of kinetic energy B show a large negative value in ($n = 1$–15, $m = 1$–10), and positive values in ($n = 1$–15, $m = 0$) and ($n = 0$, $m = 0$). This indicates kinetic energy transformations from eddy baroclinic to eddy barotropic and also to zonal barotropic components. The conversion between kinetic energy and available potential energy cannot be explicitly shown in this scheme. However, the baroclinic kinetic energy, which supports the barotropic kinetic energy, should be compensated by energy conversion from eddy available potential energy in the eddy baroclinic components ($n = 1$–15, $m = 1$–10). Finally, net energy dissipations take place as indicated by negative net D values. These results are consistent with earlier analyses by Wiin-Nielsen (1962) and Smagorinsky (1963) concerning the baroclinic and barotropic conversions. In his formulation of mean-shear flow interaction, Wiin-Nielsen assumed $\omega = 0$ at the lower surface in order to suppress the available potential energy transformation into eddy barotropic components. Although ω is not zero at the surface in the normal mode energetics, the transformation is similarly suppressed by the assumption of vanishing surface wind.

There is a significant seasonal difference of the global energy variables as shown in Table 2, which is consistent with previous findings by Kung and Tanaka (1983). The comparison of energetics variables between the seasons indicates that the small zonal barotropic energy in DJF increases to a maximum in JJA and the large zonal baroclinic energy in DJF decreases to a minimum in JJA. Zonal eddy energy and energy interactions show enhanced eddy activities in DJF as compared to JJA. In view of Kung and Tanaka's results, the seasonal differences of the global energy are caused by the larger seasonal contrast in the Northern Hemisphere rather than in the Southern Hemisphere. Despite the large seasonal variation, the signs of energy interactions and diabatic processes are consistent throughout the seasons.

An overall flow of normal mode energy during the FGGE year is shown in a box diagram in Fig. 4. The four boxes represent the energy levels of baroclinic (upper boxes) and barotropic (lower boxes) components of zonal (left boxes) and eddy (right boxes) energies. For the barotropic energy the kinetic energy of the vertical mean flow dominates. The kinetic energy of the vertical shear flow is generally associated with the existence of available potential energy through the thermal wind relation, with their sums seen as the total baroclinic energy. The flow pattern of normal mode energy, as shown in Fig. 4, is the net energy input and output of processes B, C and D as shown in the annual mean budget in Table 2. There is a net generation of zonal baroclinic energy by the differential heating, with this energy being the initial energy input into the system. The zonal baroclinic energy is first transformed into eddy baroclinic energy through transformation of zonal available potential energy to eddy available potential energy, which is further converted into eddy kinetic energy of the vertical shear flow within the box for eddy baroclinic energy. The eddy baroclinic energy is then transformed into eddy and zonal barotropic energies by the nonlinear interactions of kinetic energy. Finally, the net energy dissipations take place with zonal and eddy barotropic components and with the eddy baroclinic components.

In constructing the diagram in Fig. 4, B of the zonal baroclinic component and C of the barotropic components are not considered since their magnitude is small and their direction is uncertain. Thus, the energy flow shown in Fig. 4 is the basic flow pattern that dominates the normal mode energetics, rather than a detailed description of the transformation.

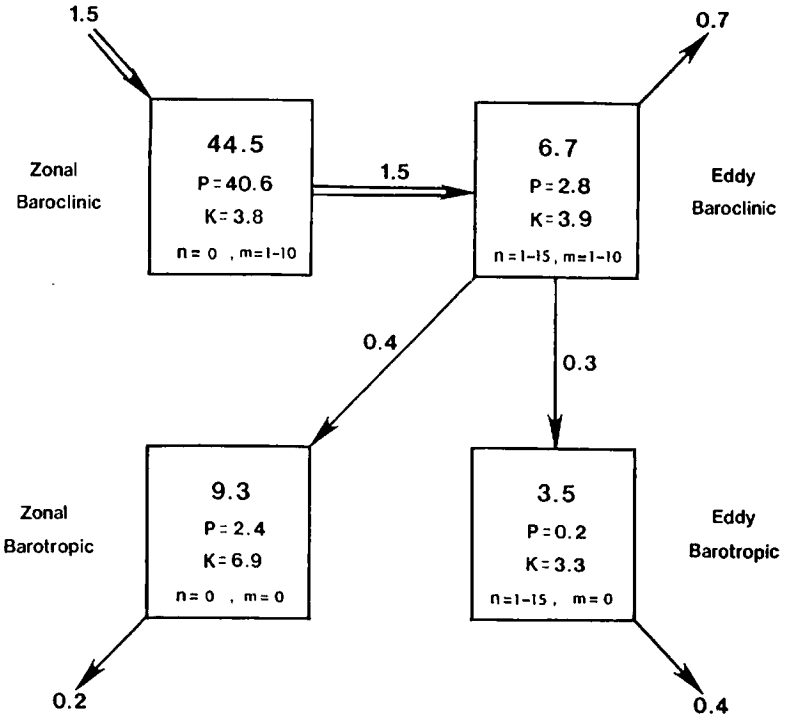

FIG. 4. Energy flow diagram by the barotropic and baroclinic decomposition of zonal energy and eddy energy. Energies are in units of 10^5 J m^{-2} and transformations in W m^{-2}. Energy flows of available potential energy are distinguished by double arrows, and those of kinetic energy by single arrows.

4. Stationary and transient components

A complex-valued coefficient of an arbitrary meteorological field may be partitioned into

$$Q(t) = Q_S + Q_A(t) + Q_T(t), \tag{9}$$

where Q_S is the time mean (stationary component), $Q_A(t)$ the annual variation (annual cycle), and $Q_T(t)$ the transient component. After subtracting Q_S from $Q(t)$, the annual cycle is obtained as the first harmonic of the one-year time series. The residual $Q_T(t)$ of Eq. (9) is then considered as the transient component. The annual mean energies, given by the quadratic term of $Q(t)$, thus can be partitioned into contributions from the terms on the right-hand side of the equation. The resulting components of the energy levels in the normal mode and standard spectral energetics are compared in Table 3 for zonal (n = 0) and eddy (n = 1–15) components. The values of the normal mode energies are the summation of m = 0 to 10. The smaller P and larger K found in the normal mode energetics as compared to those in the standard spectral energetics are a common feature for the zonal and eddy components, and this is also true for the stationary, annual and transient components. The total energy $E = K + P$ is in close agreement in both schemes, and about 90% of the zonal energy resides in the stationary component, whereas about 75% of the eddy energy resides in the transient component for both schemes. The stationary and transient energies seem to be projected reasonably onto the basis functions.

Table 4 lists the normal mode energies and transformations in the wavenumber and vertical index domains during the FGGE year partitioned into contributions from stationary components, annual variations, and transient components. For available potential energy P, and consequently for the total energy E, the largest value is found in the stationary part of the zonal baroclinic component. For kinetic energy, however, large values of K are found in the stationary barotropic and baroclinic parts of the zonal mean component, and in the transient barotropic and baroclinic parts of the zonal eddy component.

The major source of kinetic energy for nonlinear interactions is found in the eddy baroclinic component of the transient motion as indicated by the large negative B value. The kinetic energy is transferred into the eddy barotropic component of the transient motion and the zonal mean barotropic component of the stationary motion, as indicated by the large positive values. Contrary to the kinetic energy, the nonlinear interaction C supplies available potential energy mainly from the source (the zonal mean baroclinic component of the stationary motion) to the eddy baroclinic component of the transient motion. Thus, the gain of available potential energy in the eddy baroclinic transient motion supports the source of nonlinear kinetic energy transfer in this component of the circulation. The net

TABLE 3. Kinetic energy K, available potential energy P, and total energy E ($=K + P$) for the zonal ($n = 0$) and eddy ($n = 1$–15) components for the normal mode and standard spectral energetics. The annual mean energy, in unit of 10^5 J m^{-2} is partitioned into contributions from stationary fields, annual variations, and transient fields.

	Normal mode energies			Standard spectral energies		
n	K	P	E	K	P	E
			Stationary Component			
0	9.2	37.7	46.9	6.3	42.4	48.7
1–15	0.8	0.5	1.4	0.6	1.1	1.7
			Annual Variation			
0	1.1	5.1	6.2	0.8	5.6	6.4
1–15	0.5	0.3	0.9	0.3	0.8	1.1
			Transient Component			
0	0.4	0.3	0.7	0.3	0.4	0.7
1–15	5.8	2.1	7.8	5.2	3.3	8.4

diabatic process D represents an energy source in the zonal mean baroclinic component of the stationary motion, while it also represents energy sinks in both the zonal mean barotropic component of the stationary motion and the eddy barotropic and baroclinic components of the transient motion. Such a net energy input into the general circulation should reflect, for the most part, a generation of available potential energy and a net energy sink by the dissipation of kinetic energy in those components of the circulation field.

TABLE 4. Stationary components, annual variations, and transient components of the annual mean normal mode energy budget during the FGGE year (see Table 2). Energy (K, P, and E) in unit of 10^5 J m^{-2} and energy transformations (B, C, and D) in W m^{-2} are listed for the zonal ($n = 0$) and eddy ($n = 1$–15) components by the barotropic ($m = 0$) and baroclinic ($m = 1$–10) decomposition.

n	m	K	P	E	B	C	D
				Stationary Component			
0	0	6.1	1.9	8.0	0.36	−0.15	−0.21
0	1–10	3.1	35.8	38.9	−0.03	−1.37	1.40
1–15	0	0.3	0.0	0.4	−0.01	0.01	0.00
1–15	1–10	0.5	0.5	1.0	−0.11	0.12	−0.02
				Annual Variation			
0	0	0.6	0.5	1.1	0.01	−0.01	0.00
0	1–10	0.5	4.6	5.1	−0.04	−0.15	0.19
1–15	0	0.2	0.0	0.2	−0.01	0.00	0.01
1–15	1–10	0.3	0.3	0.7	−0.05	0.01	0.04
				Transient Component			
0	0	0.2	0.0	0.2	0.02	0.00	−0.02
0	1–10	0.2	0.3	0.5	−0.01	0.03	−0.02
1–15	0	2.8	0.1	2.9	0.34	0.08	−0.42
1–15	1–10	3.0	2.0	4.9	−0.60	1.31	−0.72

Figure 5 compares the spectral distributions of energy for the transient component of the motion E_T and the sum of E_S and E_A, i.e., the energies associated with the stationary component and annual variation of the motion, respectively. The same spectral distributions obtained by the standard spectral energetics are also shown as dashed lines for comparison. The two energetics schemes indicate similar spectral distributions in the zonal wavenumber domain, except for a bias toward lower energy levels in the normal mode scheme as was mentioned above. The energy level of E_T is one order larger than that of ($E_S + E_A$) for wavenumbers greater than 5, indicating the dominance of transient waves for synoptic-scale circulation.

The components of the individual vertical indices from $m = 0$ to 5 in the transient kinetic energy K_T and transient available potential energy P_T are presented in Fig. 6 as functions of the zonal wavenumber. The results show the dominant barotropic kinetic energy ($m = 0$) for all zonal wavenumbers. The baroclinic index $m = 4$ provides the largest contribution to P_T. The first internal index $m = 1$ indicates relatively high energy levels at wavenumbers 1 and 2 of K_T, reflecting

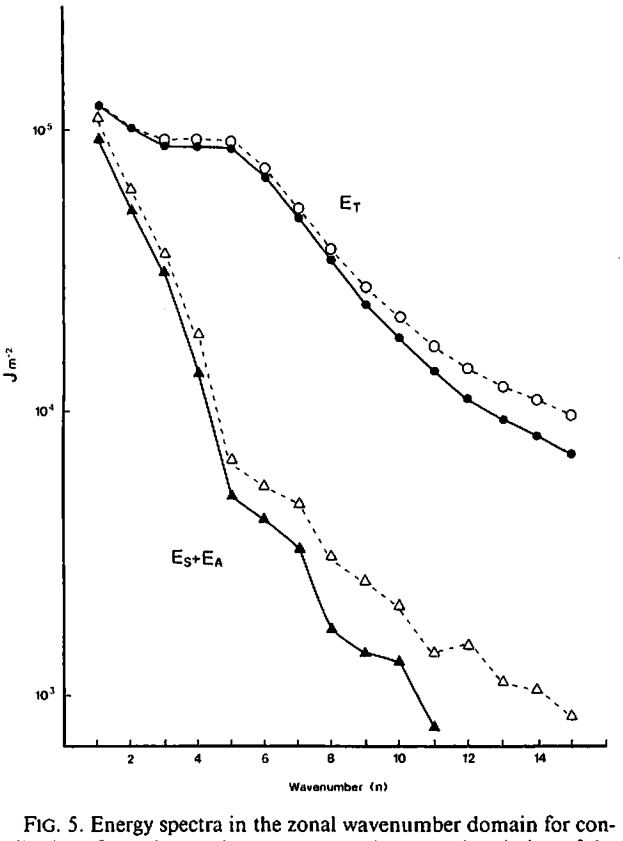

FIG. 5. Energy spectra in the zonal wavenumber domain for contributions from the steady component, plus annual variation of the motion ($E_S + E_A$) and transient motion E_T. The normal mode energetics are solid lines, and the standard spectral energetics are dashed lines.

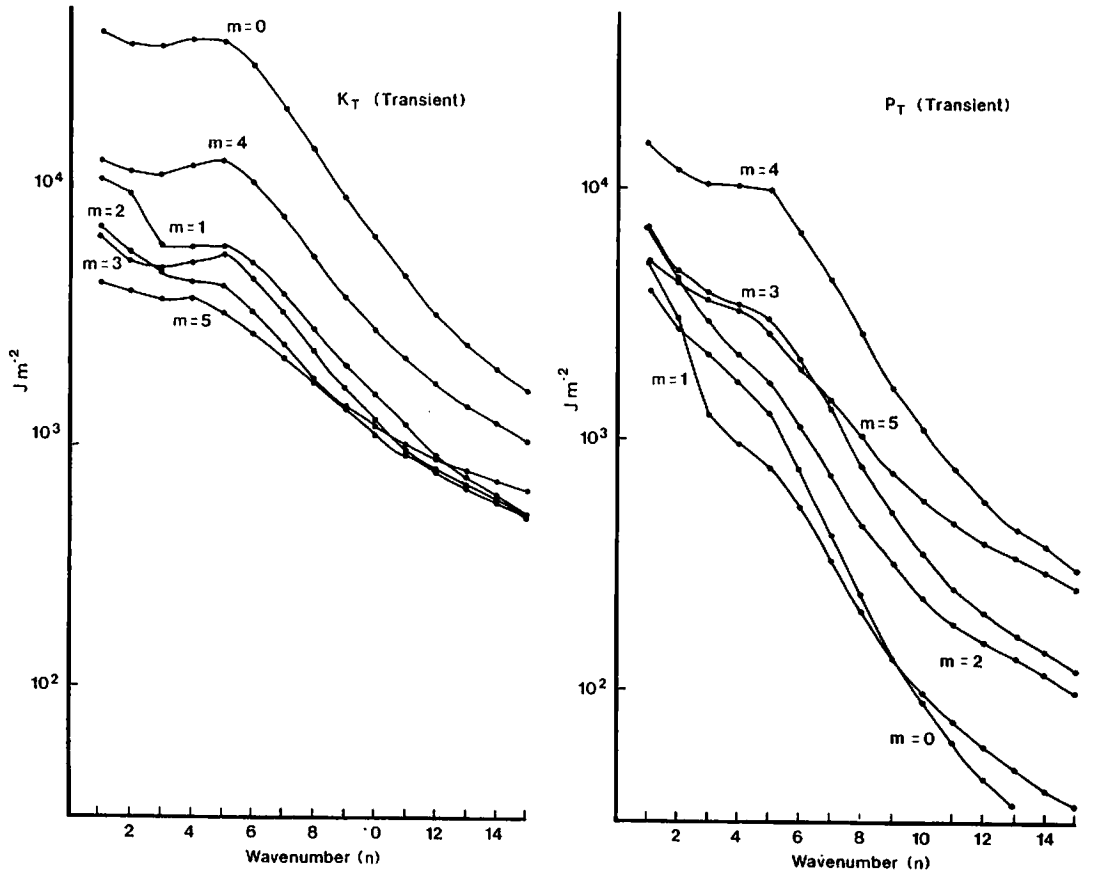

FIG. 6. Spectral distribution of transient kinetic energy K_T and transient available potential energy P_T in the zonal wavenumber domain for contributions from the individual vertical indices $m = 0$ to 5.

the occasional amplification and vertical propagation into the stratosphere.

The kinetic energy interaction B corresponds to $(L - M)$ in the standard spectral energetics scheme (see Kung and Tanaka 1983; Saltzman 1970), where L is the wave–wave interaction and M the wave–mean interaction of kinetic energy in the zonal wavenumber domain. Likewise, the available potential energy interaction C is equivalent to $(S + R)$ in the standard spectral scheme, where S and R are the wave–wave and mean–wave interactions of available potential energy, respectively. The spectral distributions of B and C are compared in Fig. 7 with those of $(L - M)$ and $(S + R)$ (shown as dashed lines), computed from the same GFDL dataset by Kung (1986). As seen in the figure, the energy interactions in the two energetics schemes show nearly identical spectral distributions. The positive values of C and $(S + R)$ at all wavenumbers indicate the transformation of zonal mean available potential energy to eddy available potential energy, whereas the negative values of B and $(L - M)$ show the transformation of eddy kinetic energy to the zonal mean component. As was discussed with Table 4, most of these eddy energy transformations are associated with the transient motion of the general circulation. In Fig. 7 the spectral distributions of the kinetic energy transformation due to the transient motion are presented for individual vertical indices of $m = 0$–5. It is clearly shown that the kinetic energy source (indicated by a negative B_T value) is in the baroclinic components to support the supply of kinetic energy, the largest of which is at $m = 4$, centered at the wavenumber $n = 6$. In contrast, the barotropic component shows positive B_T values, supporting the sink of kinetic energy through dissipation (see Table 4). With the results in Fig. 7 and Table 4, there should be a net up-scale energy cascade from baroclinic components of synoptic waves to the barotropic components of long waves and the zonal mean. The same spectral distributions are illustrated in Fig. 7 for the available potential energy transformations for the transient motion C_T. A large positive C_T is seen in $m = 4$, centered at $n = 6$, implying that the largest supply of available potential energy is in this range. This energy transformation can be regarded as a characteristic of the atmospheric baroclinic instability (Charney 1947), by which the synoptic waves gain energy from the zonal available potential energy. As mentioned in the preceding section, the baroclinic conversion (that reaches its maximum at the largest baroclinic instability) relating the available potential energy and kinetic energy cannot be analyzed explicitly in the present normal mode scheme. It is a part of the

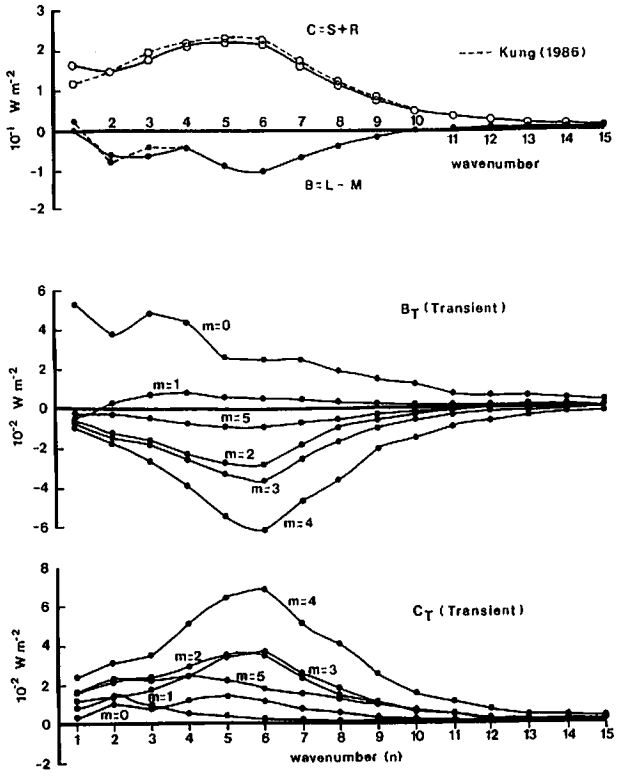

FIG. 7. Spectral distributions of nonlinear energy transformations in the zonal wavenumber domain in the normal mode scheme (solid lines) and the standard spectral energetics scheme after Kung (1986) (dashed lines). Also, transient parts of nonlinear energy transformations B_T and C_T are partitioned in the contributions from the individual vertical indices $m = 0$ to 5.

residual processes which appears as a compensation of the negative B_T with the positive C_T in the baroclinic components. This result appears reasonable, and agrees with existing studies (e.g., Smagorinsky 1963; Wiin-Nielsen 1962).

5. A winter time series analysis

The box diagram in Fig. 4 only provides information about net energy transformations. In order to trace the paths of energy transformations, time series analyses of normal mode energy and energy transformations are presented for the FGGE winter. Figure 8 illustrates the temporal variations of barotropic ($m = 0$) and baroclinic ($m = 3$–10) energies for zonal mean motion ($n = 0$), ultralong waves ($n = 1$–2), and synoptic waves ($n = 3$–15) over the Northern Hemisphere during the FGGE winter. The energetics variables of barotropic and baroclinic components are evaluated using the vertical and Fourier transforms of variables over the hemisphere without the Hough transform. A three-day running mean is applied to the results. The vertical indices $m = 1$ and 2 are excluded from the computation of baroclinic energy to eliminate the influence of stratospheric variations. It is shown in Tanaka et al. (1986) that, resulting from the occasional vertical propagation of planetary waves, the variation of $m = 1$ is distinctly different from other vertical indices.

The time variation of zonal baroclinic energy ($n = 0$, $m = 3$–10) indicates clear energy peaks on 16 and 28 December and 9 January superimposed on the seasonal trends. As is expected from Fig. 4, subsequent increases in the baroclinic energy of synoptic waves can be seen in the time series ($n = 3$–15, $m = 3$–10) through a process of atmospheric baroclinic instability. The time lag is about 5 days. Although not shown in the figure, the time variation of synoptic-scale barotropic energy ($n = 3$–15, $m = 0$) is almost in phase with its baroclinic energy variation, implying that the instability process excites both of the barotropic and baroclinic energies in synoptic eddies. The barotropic energy of ultralong waves ($n = 1$–2, $m = 0$) increases 3 days later through the wave–wave interaction of kinetic energy. Finally, the baroclinic energy of planetary waves increases after 3 days following its barotropic energy peaks. We should note that the zonal barotropic energy ($n = 0$, $m = 0$) remains almost constant through the entire period.

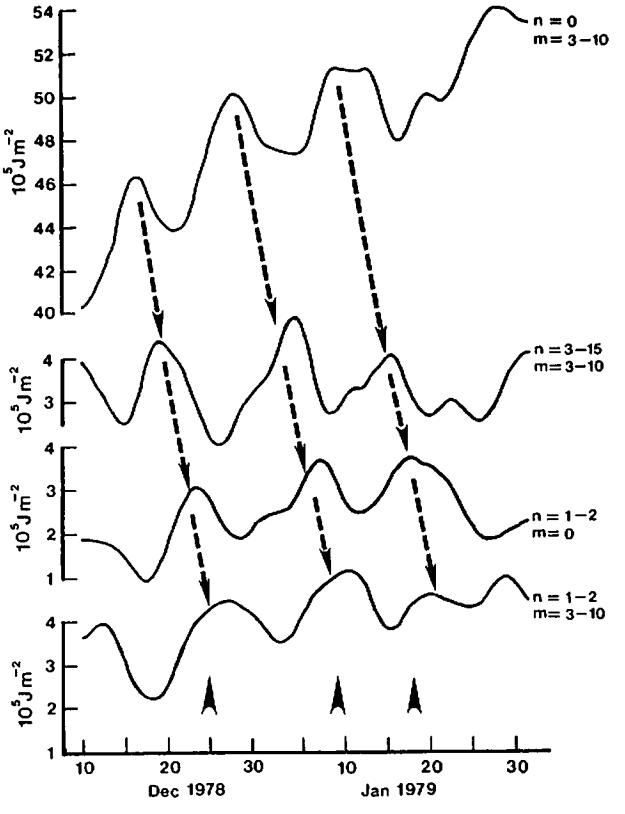

FIG. 8. Time change of barotropic ($m = 0$) and baroclinic ($m = 3$–10) energies for zonal mean motion ($n = 0$), ultralong waves ($n = 1$–2), and synoptic waves ($n = 3$–15) over the Northern Hemisphere from 10 December 1978 through 31 January 1979. Appearances of typical Rex blockings (after Kung and Baker 1986) are marked by arrows over the time axis.

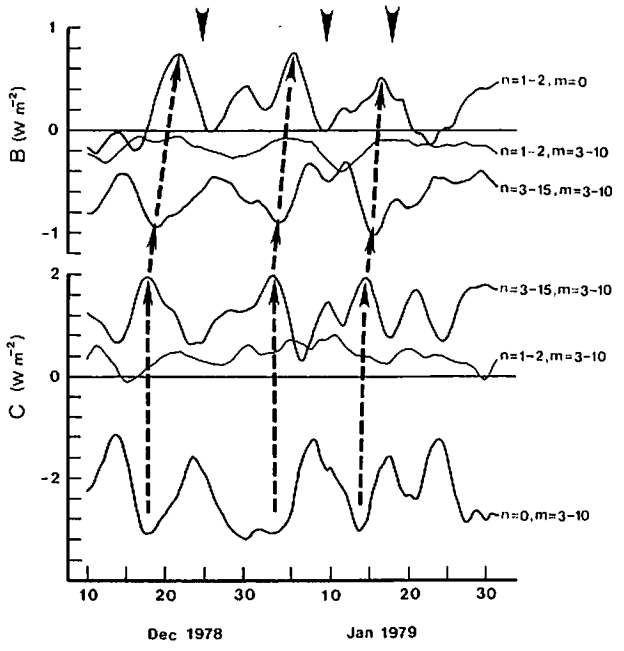

FIG. 9. Time change of kinetic energy transformations B and available potential energy transformations C for the corresponding energy terms in Fig. 8. Appearances of typical blockings after Kung and Baker (1986) are marked by the arrows at the top of the diagram.

Time changes of kinetic energy transformation B and available potential energy transformation C are illustrated in Fig. 9 for the energy components examined above. The values are a 3-day running mean of the original time series computed over the Northern Hemisphere. The transformation C clearly indicates the process of atmospheric baroclinic instability from zonal to synoptic-scale baroclinic energy (lower arrows). The time variation in Fig. 8 is consistent with the time variation of C. Baroclinic conversion of available potential energy to kinetic energy, which is described by the positive C and negative B in synoptic waves, shows clear links with each other (middle arrows). When the baroclinic waves decay, the up-scale kinetic energy cascade occurs from the synoptic waves to barotropic component of ultra-long waves (upper arrows). The time series as shown in Fig. 9 are consistent with the sequence of energy flows from zonal baroclinic components, via synoptic-scale baroclinic waves, to the barotropic components of ultra-long waves as summarized in Figs. 4 and 7.

It is interesting to note here that the up-scale kinetic energy cascade from synoptic waves to ultra-long waves supports the major energy source of the Atlantic blocking around December 25 (Hansen and Chen 1982) and Pacific blocking around January 9 (Kung and Baker 1986) (see the arrows above the time axis in Figs. 8 and 9). The present time series analysis shows that such an up-scale kinetic energy cascade is accompanied by energy transformations from baroclinic to barotropic components. Since the blocking phenomenon is often characterized by its barotropic structure, the barotropic and baroclinic decomposition of normal mode energetics in this study may provide additional information in the study of blocking phenomena.

6. Concluding remarks

The energetics characteristics of the global atmospheric circulation during the FGGE year are examined using the three-dimensional normal mode expansions, and are summarized in the barotropic and baroclinic components of the stationary and transient flows of the general circulation.

There is a net energy generation by the differential heating in the zonal baroclinic energy. The zonal baroclinic energy is transformed into eddy baroclinic energy by a process of atmospheric baroclinic instability. After the conversion of available potential energy to kinetic energy in the baroclinic components of the synoptic-scale waves, the synoptic-scale baroclinic energy is transformed into the barotropic energy of the planetary waves by way of the up-scale wave–wave interactions of kinetic energy. Similarly, the eddy baroclinic energy is transformed into zonal barotropic energy. The zonal mean kinetic energy thus maintains its barotropic structure by the activity of baroclinic waves. Although the seasonal variability of the global energetics results is noticeable, the signs of energy transformations are consistent throughout the year. The analysis also indicates that the available potential energy is transformed from the stationary baroclinic part to the transient baroclinic part, whereas the kinetic energy is transformed from transient baroclinic parts to the stationary barotropic part.

Time series analysis of the Northern Hemisphere winter energetics variables supports the above results, exhibiting a sequence of energy transformations from the zonal baroclinic components, via synoptic-scale baroclinic components, to planetary-scale barotropic components.

A comparison of the energetics in the normal mode and standard spectral schemes indicates that the nonlinear energy transformations in these two schemes are similar. Thus, the normal mode energetics diagnosis may supplement the standard spectral energetics in the zonal wavenumber domain with specific energetics information that is not possible in the standard scheme.

Acknowledgments. The authors gratefully acknowledge the technical assistance rendered by C. Baker, K. Milburn, V. Peters, and G. D. Vickers. They are also indebted to Dr. Y. Hayashi, Dr. I. M. Held, and Dr. A. Kasahara who provided thorough, constructive reviews in the revision of the original manuscript. This research was supported by the National Oceanic and Atmospheric Administration under NOAA Grants NA86AA-D-AC114 and NA88AA-D-AC103.

APPENDIX

Description of Normal Mode Energetics Scheme

A system of primitive equations in a pressure coordinate may be reduced to three prognostic equations of horizontal motions and thermodynamics with three dependent variables (u, v, ϕ). Using a matrix notation, these primitive equations (Tanaka 1985) may be written in a compact form:

$$\mathbf{M}\frac{\partial}{\partial t}\mathbf{W} + \mathbf{L}\mathbf{W} = \mathbf{B} + \mathbf{C} + \mathbf{D}, \tag{A1}$$

where

$$\mathbf{W} = (u, v, \phi)^{\mathrm{T}}, \tag{A2}$$

$$\mathbf{M} = \mathrm{diag}\left(1, 1, -\frac{\partial p^2 \partial}{\partial p R\gamma \partial p}\right), \tag{A3}$$

$$\mathbf{L} = \begin{bmatrix} 0 & -2\Omega\sin\theta & \dfrac{1\partial}{a\cos\theta\partial\lambda} \\ 2\Omega\sin\theta & 0 & \dfrac{1\partial}{a\partial\theta} \\ \dfrac{1\partial}{a\cos\theta\partial\lambda} & \dfrac{1\partial(\ )\cos\theta}{a\cos\theta\partial\theta} & 0 \end{bmatrix}, \tag{A4}$$

$$\mathbf{B} = \begin{bmatrix} -\mathbf{V}\cdot\nabla u - \omega\dfrac{\partial u}{\partial p} + \dfrac{\tan\theta}{a}uv \\ -\mathbf{V}\cdot\nabla v - \omega\dfrac{\partial v}{\partial p} - \dfrac{\tan\theta}{a}uu \\ 0 \end{bmatrix}, \tag{A5}$$

$$\mathbf{C} = \begin{bmatrix} 0 \\ 0 \\ \dfrac{\partial}{\partial p}\left[\dfrac{p}{\gamma}\left(-\mathbf{V}\cdot\nabla T - \omega\dfrac{\partial T}{\partial p}\right)\right] \end{bmatrix}, \tag{A6}$$

$$\mathbf{D} = \left[F_u, F_v, \frac{\partial}{\partial p}\left(\frac{pQ}{c_p\gamma}\right)\right]^{\mathrm{T}}. \tag{A7}$$

Refer to Appendix of Tanaka (1985) and Table 1 for symbols, definitions, and variables. A scaling of $T_0 \gg T$ has been introduced in the equation of thermodynamics (see Holton 1975).

The three-dimensional normal mode functions $\Pi_{nlm}(\lambda, \theta, p)$ are obtained as eigensolutions of the homogeneous equation (A1) putting zero for the right hand side (see Kasahara and Puri 1981). They are given by a tensor product of vertical structure functions and Hough harmonics. It is known that they form a complete set of expansion basis and satisfy an orthonormality condition under an inner product $\langle\ ,\ \rangle$ as:

$$\langle \Pi_{nlm}, \Pi_{n'l'm'} \rangle = \frac{2}{p_s S}\int_S \int_0^{p_s} \Pi^*_{nlm}\cdot\Pi_{n'l'm'}\,dp dS = \delta_{nn'}\delta_{ll'}\delta_{mm'}, \tag{A8}$$

where the surface pressure p_s is treated as a constant near the earth's surface.

In order to obtain spectral primitive equations, we assume in the following that the vectors in (A1) belong to a subspace spanned by the series of the 3-D NMFs. A similar assumption is already seen in the nonlinear normal mode initialization technique which provides successful initial data for the prediction models:

$$\mathbf{W}(\lambda, \theta, p, t) = \sum_{n=-\infty}^{\infty}\sum_{l=0}^{\infty}\sum_{m=0}^{\infty} w_{nlm}(t)X_m\Pi_{nlm}(\lambda, \theta, p), \tag{A9}$$

$$\mathbf{B}(\lambda, \theta, p, t) = \sum_{n=-\infty}^{\infty}\sum_{l=0}^{\infty}\sum_{m=0}^{\infty} b_{nlm}(t)Y_m\Pi_{nlm}(\lambda, \theta, p),$$

$$\mathbf{C}(\lambda, \theta, p, t) = \sum_{n=-\infty}^{\infty}\sum_{l=0}^{\infty}\sum_{m=0}^{\infty} c_{nlm}(t)Y_m\Pi_{nlm}(\lambda, \theta, p),$$

$$\mathbf{D}(\lambda, \theta, p, t) = \sum_{n=-\infty}^{\infty}\sum_{l=0}^{\infty}\sum_{m=0}^{\infty} d_{nlm}(t)Y_m\Pi_{nlm}(\lambda, \theta, p),$$

where the scaling matrices should be defined for each vertical index as:

$$X_m = \mathrm{diag}((gh_m)^{1/2}, (gh_m)^{1/2}, gh_m),$$

$$Y_m = \mathrm{diag}(2\Omega(gh_m)^{1/2}, 2\Omega(gh_m)^{1/2}, 2\Omega). \tag{A10}$$

Taking the inner product of (A1) and $Y_m^{-1}\Pi_{nlm}$, and using (A8), we obtain the three-dimensional spectral primitive equations of (1) in the text which are represented by the dimensionless expansion coefficients in (A9):

$$\frac{d}{dt}w_{nlm} + i\sigma_{nlm}w_{nlm} = b_{nlm} + c_{nlm} + d_{nlm}. \tag{A11}$$

The corresponding energy balance equations in the spectral domain are discussed in (2):

$$\frac{d}{dt}E_{nlm} = B_{nlm} + C_{nlm} + D_{nlm}. \tag{A12}$$

For the energy balance equations (2) with their descriptions (3)–(6), we can show the following identities by taking the inner product of (A1) and $(p_s/2g)\mathbf{W}$:

$$\left\langle \frac{p_s}{2g}\mathbf{W}, \mathbf{M}\frac{\partial}{\partial t}\mathbf{W}\right\rangle = \sum_{n=0}^{\infty}\sum_{l=0}^{\infty}\sum_{m=0}^{\infty}\frac{d}{dt}E_{nlm},$$

$$= \frac{d}{dt}\frac{1}{Sg}\int_S\int_0^{p_s} K + P\,dp dS + \frac{d}{dt}\frac{1}{Sg}\int_S \frac{p_s}{2RT_0}\phi_s^2\,dS, \tag{A13}$$

$$\left\langle \frac{p_s}{2g}\mathbf{W}, \mathbf{LW} \right\rangle = 0,$$

$$= \frac{1}{Sg}\int_S \int_0^{p_s} \nabla\cdot\phi\mathbf{V}\,dpdS, \quad \text{(A14)}$$

$$\left\langle \frac{p_s}{2g}\mathbf{W}, \mathbf{B} \right\rangle = \sum_{n=0}^{\infty}\sum_{l=0}^{\infty}\sum_{m=0}^{\infty} B_{nlm},$$

$$= \frac{1}{Sg}\int_S \int_0^{p_s} -\nabla\cdot K\mathbf{V} - \frac{\partial K\omega}{\partial p}\,dpdS, \quad \text{(A15)}$$

$$\left\langle \frac{p_s}{2g}\mathbf{W}, \mathbf{C} \right\rangle = \sum_{n=0}^{\infty}\sum_{l=0}^{\infty}\sum_{m=0}^{\infty} C_{nlm},$$

$$= \frac{1}{Sg}\int_S \int_0^{p_s} -\nabla\cdot P\mathbf{V} - \frac{\partial P\omega}{\partial p}\,dpdS + \frac{1}{Sg}\int_S \frac{p_s\phi_s}{\gamma}\left(-V\cdot\nabla T - \omega\frac{\partial T}{\partial p}\right)_s dS, \quad \text{(A16)}$$

$$\left\langle \frac{p_s}{2g}\mathbf{W}, \mathbf{D} \right\rangle = \sum_{n=0}^{\infty}\sum_{l=0}^{\infty}\sum_{m=0}^{\infty} D_{nlm},$$

$$= \frac{1}{Sg}\int_S \int_0^{p_s} uF_u + vF_u + \frac{RT}{\gamma c_p}Q\,dpdS + \frac{1}{Sg}\int_S \frac{p_s\phi_s}{\gamma}Q_s\,dS, \quad \text{(A17)}$$

where the subscript s denotes the variables at $p = p_s$. The dimensional factor of $p_s/2g$ is multiplied for the inner products, so that the energy is expressed in a physical units of J m^{-2}. The first lines in the right hand sides of (A13)–(A17) are derived by substitutions of (A9) into the variables, using the orthonormality condition (A8) and the scaling matrices (A10). On the other hand, the second lines are the direct consequence of the substitution of (A2)–(A7) into the variables. The vertical change of the static stability parameter γ has been neglected as in Holton (1975).

The assumption of (A9) leads to the next relation which has been used in (A13):

$$\frac{\partial\phi_s}{\partial p} + \frac{\gamma}{p_s T_0}\phi_s = 0, \quad \text{at} \quad p = p_s. \quad \text{(A18)}$$

Moreover if we assume that the surface wind vanishes at the lower boundary:

$$\left(u, v, \frac{dz}{dt}\right)_s^T = 0, \quad \text{at} \quad p = p_s, \quad \text{(A19)}$$

we will obtain

$$\frac{\partial\phi_s}{\partial t} - \frac{RT_0}{p_s}\omega_s = 0, \quad \text{at} \quad p = p_s. \quad \text{(A20)}$$

Hence the surface integral in (A13) becomes

$$\frac{d}{dt}\frac{1}{Sg}\int_S \frac{p_s}{2RT_0}\phi_s^2\,dS = \frac{1}{Sg}\int_S \phi_s\omega_s\,dS, \quad \text{(A21)}$$

which is the surface integral of geopotential flux across the lower boundary. The available potential energy in the normal mode energetics involves contributions from geopotential flux. However, the observed variance of ϕ_s is only one percent of $K + P$ in the first term of (A13), and thus negligible. The second surface integrals in (A16) and (A17) should vanish in order to relate the energetics variables with those in the standard spectral energetics. One may expect the smallness of ϕ_s as well as the weak horizontal wind near the surface, disregarding the geopotential flux across the lower boundary in (A21) (see Tanaka 1985). On the other hand, it may be demonstrated that these surface integrals vanish by the assumption (A19) applied to the equation of thermodynamics with a scaling of $T_0 \gg T$. In this case the summations of B_{nlm} and C_{nlm} respectively become zero even for the nonzero ω at the lower boundary because $K\omega = 0$ there and $P\omega$ is scaled out compared to $\phi\omega$ using $T_0 \gg T$ and (A18). We choose the latter case in our present study because the surface ω is not zero in the normal mode energetics.

We have compared the energetics results for the entire FGGE year assuming (A19) and also replacing (A19) with a free-slip condition for the horizontal wind. The results are similar to the present results except for large contributions of C_{nlm} at the barotropic components for the free-slip case as seen in Tanaka (1985). The present results, which show rather small contributions of C_{nlm}, $m = 0$, agree with Wiin-Nielsen's (1962) results in that the available potential energy supports the eddy baroclinic kinetic energy. It seems that the treatment of vanishing surface wind is a reasonable assumption for the normal mode energetics. Although (A19) is a compromise to avoid the complexity near the surface, the assumption provides an energetically consistent equation set, and thus it may be acceptable for the global energetics analysis.

REFERENCES

Charney, J. G., 1947: The dynamics of long waves in a baroclinic westerly current. *J. Meteor.*, **4**, 135–163.

Eliasen, E., and B. Machenhauer, 1965: A study of the fluctuations of the atmospheric planetary flow patterns represented by spherical harmonics. *Tellus*, **17**, 220–238.

Fulton, S. R., and W. H. Schubert, 1985: Vertical normal mode transforms: Theory and application. *Mon. Wea. Rev.*, **113**, 647–658.

Hansen, A. R., and T.-C. Chen, 1982: A spectral energetics analysis of atmospheric blocking. *Mon. Wea. Rev.*, **110**, 1146–1165.

Hayashi, Y., and D. G. Golder, 1983: Transient planetary waves simulated by GFDL spectral general circulation models. Part II: Effect of nonlinear energy transfer. *J. Atmos. Sci.*, **40**, 951–957.

Holmström, I., 1963: On a method for parametric representation of the state of the atmosphere. *Tellus*, **15**, 127–149.

Holton, J. R., 1975: The Dynamic Meteorology of the Stratosphere

and Mesosphere. *Meteor. Monogr.*, 37, Amer. Meteor. Soc., 218 pp.

Kasahara, A., and K. Puri, 1981: Spectral representation of three-dimensional global data by expansion in normal mode functions. *Mon. Wea. Rev.*, **109**, 37–51.

Kung, E. C., 1986: Spectral energetics of the global circulation during the FGGE year. *Proc. Natl. Conf. on the Scientific Results of the First GARP Global Experiment*, Amer. Meteor. Soc., pp. 84–87. [May be obtained from American Meteorological Society.]

——, and W. E. Baker, 1986: Spectral energetics of the observed and simulated northern hemisphere general circulation during blocking episodes. *J. Atmos. Sci.*, **43**, 2792–2812.

——, and H. Tanaka, 1983: Energetics analysis of the global circulation during the special observation periods of FGGE. *J. Atmos. Sci.*, **40**, 2575–2592.

Miyakoda, K., J. Sheldon and J. Sirutis, 1982: Four-dimensional analysis experiment during the GATE period. Part II. *J. Atmos. Sci.*, **39**, 486–506.

Ploshay, J. J., R. K. White and K. Miyakoda, 1983: FGGE IIIb daily global analyses. Part I. NOAA Date Rep., ERL GFDL-1. GFDL, Princeton, N.J., 278 pp. [May be obtained from GFDL/NOAA, Princeton University.]

Saltzman, B., 1957: Equations governing the energetics of the larger scales of atmospheric turbulence in the domain of wavenumber. *J. Meteor.*, **14**, 513–523.

——, 1970: Large-scale atmospheric energetics in the wavenumber domain. *Rev. Geophys. Space Phys.*, **8**, 289–302.

Sasaki, Y. K., and L. P. Chang, 1985: Numerical solution of the vertical structure equation in the normal mode method. *Mon. Wea. Rev.*, **113**, 782–793.

Smagorinsky, J., 1963: General circulation experiments with the primitive equations. I. The basic experiment. *Mon. Wea. Rev.*, **91**, 99–164.

Staniforth, A., M. Béland and J. Côrté, 1985: An analysis of the vertical structure equation in sigma coordinates. *Atmos. Ocean.*, **23**, 323–358.

Tanaka, H., 1985: Global energetics analysis by expansion into three-dimensional normal mode functions during the FGGE winter. *J. Meteor. Soc. Japan*, **63**, 180–200.

——, E. C. Kung and W. E. Baker, 1986: Energetics analysis of the observed and simulated general circulation using three-dimensional normal mode expansions. *Tellus*, **38**, 412–428.

Tenenbaum, J., 1976: Spectral and spatial energetics of the GISS model atmosphere. *Mon. Wea. Rev.*, **104**, 15–30.

Wiin-Nielsen, A., 1962: On transformation of kinetic energy between the vertical shear flow and the vertical mean flow in the atmosphere. *Mon. Wea. Rev.*, **90**, 311–323.